Reionization of the Local Group of Galaxies

Article (Published Version)

Monthly Notices of the ROYAL ASTRONOMICAL SOCIETY

Mon. Not. R. Astron. Soc. **413,** 2093–2102 (2011) doi:10.1111/j.1365-2966.2011.18292.x

Reionization of the Local Group of galaxies

Ilian T. Iliev,[1,2]★ Ben Moore,[2] Stefan Gottlöber,[3] Gustavo Yepes,[4] Yehuda Hoffman[5] and Garrelt Mellema[6]

[1]*Astronomy Centre, Department of Physics & Astronomy, Pevensey II Building, University of Sussex, Falmer, Brighton BN1 9QH*
[2]*Universität Zürich, Institut für Theoretische Physik, Winterthurerstrasse 190, CH-8057 Zürich, Switzerland*
[3]*Astrophysical Institute Potsdam, An der Sternwarte 16, 14482 Potsdam, Germany*
[4]*Universidad Autónoma de Madrid, Grupo de Astrofisica, 28049 Madrid, Spain*
[5]*Racah Institute of Physics, Hebrew University, Jerusalem 91904, Israel*
[6]*Stockholm University, SE-106 91 Stockholm, Sweden*

Accepted 2011 January 2. Received 2010 December 4; in original form 2010 May 18

ABSTRACT

We present the first detailed structure formation and radiative transfer simulations of the reionization history of our cosmic neighbourhood. To this end, we follow the formation of the Local Group of galaxies and nearby clusters by means of constrained simulations, which use the available observational constraints to construct a representation of those structures which reproduces their actual positions and properties at the present time. We find that the reionization history of the Local Group is strongly dependent on the assumed photon production efficiencies of the ionizing sources, which are still poorly constrained. If sources are relatively efficient, i.e. the process is 'photon-rich', the Local Group is primarily ionized externally by the nearby clusters. Alternatively, if the sources are inefficient, i.e. reionization is 'photon-poor' the Local Group evolves largely isolated and reionizes itself. The mode of reionization, external versus internal, has important implications for the evolution of our neighbourhood, in terms of e.g. its satellite galaxy populations and primordial stellar populations. This therefore provides an important avenue for understanding the young universe by detailed studies of our nearby structures.

Key words: radiative transfer – methods: numerical – galaxies: formation – galaxies: high-redshift – intergalactic medium – cosmology: theory.

1 INTRODUCTION

Approximately thirteen billion years ago the cosmic neighbourhood destined eventually to become our Local Group (LG) of galaxies underwent a dramatic transition: a giant ionization front swept through, engulfing it in a sea of ionizing radiation. This occurred as a local manifestation of a global transition of the intergalactic medium in the whole universe referred to as cosmic reionization, caused by the radiation from the first galaxies. This process converted the intergalactic medium from neutral and cold gas during the cosmic dark ages before any galaxies existed, into a hot, ionized plasma.

The absorption spectra of quasi-stellar objects (QSOs) from redshift 0 to about 6 show that the intergalactic medium has been almost fully ionized for most of the lifetime of the Universe. On the other hand, the recent data from the *Wilkinson Microwave Anisotropy Probe* (*WMAP*) satellite yielded a rather large optical depth for scattering the cosmic microwave background photons on free electrons. This strongly suggests that the reionization epoch started well before redshift 10 and therefore was fairly extended in time. It also confirmed independently the existence of a reionization epoch, required by this additional optical depth. The process of reionization had far-reaching consequences for subsequent galaxy formation. The photoionization heating which accompanies reionization increased the gas temperature from very low one, of the order of a few K or less, during the cosmic dark ages before the first stars formed, to $\sim 10^4$ K or more. This in turn increased the corresponding Jeans mass, the mass above which gas pressure cannot successfully counteract gravity, by about five orders of magnitude. This strongly suppressed the formation of low-mass galaxies and cut off the star formation in previously formed ones, and thereby should have significantly influenced the early population of dwarf satellite galaxies. For this reason, reionization is often invoked as a plausible explanation for the observed lack of galaxy satellites compared to the numbers predicted by pure dark matter simulations (Bullock, Kravtsov & Weinberg 2000; Muñoz et al. 2009; Busha et al. 2010; Macciò et al. 2010). The same ionization and heating process also changed significantly the character of star formation, as stars whose

★E-mail: i.t.iliev@sussex.ac.uk

formation starts out from hot, ionized gas, even those with a primordial element abundance, are different from the ones forming out of initially cold gas (e.g. Mackey, Bromm & Hernquist 2003).

In recent years a variety of theoretical and numerical modelling work has shown that reionization was highly patchy in nature, with a very large variation in the times at which different regions become reionized (e.g. Iliev et al. 2006a, 2007; Zahn et al. 2007). Many of the effects of reionization on the later structure formation are highly dependent on the stage at which the forming structures are at the time when they become reionized. Therefore, it is important to follow the reionization history of different patches in detail and to compare the timing of reionization with the stage of formation of the local structures.

Weinmann et al. (2007) used large-scale reionization simulations to study the reionization history of galaxies of a variety of present-day types: field galaxies, cD central cluster galaxies, L_* galaxies and LG-like systems. In particular, they focused on the question which galaxies are reionized internally (i.e. by their own progenitors) versus externally (i.e. before significant fraction of their mass is in collapsed objects). For most galaxy types the answer is statistical, with certain probabilities for each outcome. They found that there is a halo mass scale, of the order of $10^{12}\,\mathrm{M}_{\odot}$, which divides the massive galaxies which are predominantly internally reionized and lower mass ones for which the opposite is true. More recently, Alvarez et al. (2009) studied the same problem using larger-scale, coarsely resolved semi-analytical reionization calculations. They achieved better statistics for the larger haloes, from Milky Way sized up to galaxy clusters, as a consequence of the larger volume their calculation followed and reached very similar conclusions to Weinmann et al. (2007).

However, these previous studies are statistical and therefore can only yield a certain probability for a given type of system to be externally or internally reionized. In contrast, the answer for a specific system, like our own LG of galaxies, consisting of the Milky Way, Andromeda, M33 and their satellite galaxies, will depend on the details of its and its neighbouring systems' formation, the timing of that formation and the relative positions in space of their progenitors at the relevant epochs. This kind of detailed information can only be obtained through numerical simulations with constrained initial conditions.

Constrained simulations aim to reproduce the spatial and velocity structure of our LG and its neighbourhood at present (redshift $z = 0$). In this work we combine the most advanced constrained realizations of the LG available at present with an accurate treatment of the radiative transfer during cosmic reionization. This allowed us for the first time to calculate the specific reionization history of all LG progenitors, as well as those of the nearby structures like the Virgo and Fornax clusters of galaxies.

2 METHODOLOGY

2.1 Constrained simulations of the local universe

The optimal way of constructing a numerical simulation that closely reproduces our local cosmological neighbourhood is provided by the Hoffman & Ribak (1991) algorithm for making a constrained realizations of Gaussian random field. Given our ability to extract observational data that can be imposed as linear constraints on the primordial perturbation field, this method can be used to construct initial conditions that obey these constraints. Here we follow Klypin et al. (2003) and impose two types of data on the simulation. The first data set consists of peculiar velocities of galaxies, drawn from the MARK III (Willick et al. 1997), surface brightness fluctuation (Tonry et al. 2001) catalogues and the Catalogue of Nearby Galaxies (Karachentsev et al. 2004). The other data set is obtained from the catalogue of nearby X-ray-selected clusters of galaxies (Reiprich & Böhringer 2002). The main obstacle faced here is how to translate the present epoch observables into quantities that are linear in the primordial perturbation fields. Peculiar velocities evolve more slowly than the density field and are assumed here to be linear. The present epoch virial parameters of the clusters are processed by the spherical top-hat model to produce their linear overdensity. The data used here and its associated observational errors effectively constrain the large-scale structure (LSS) on scales larger than $\approx 5\,h^{-1}$ Mpc (cf. Klypin et al. 2003). The simulation used here is designed to reproduce the Local Supercluster, harbouring a Virgo-like cluster. Such a configuration is easily reproduced by the constrained simulations. LG-like objects, on the other hand, are randomly emerging in the simulations. The simulations used here were each selected out of a few to have a LG-like object, similar to the observed one. They are described in more detail in Gottlöber, Hoffman & Yepes (2010).

Starting from the above constrained initial conditions, the GADGET-2 code (Springel 2005) was used to follow the dark matter in a $L = 64\,h^{-1}$ Mpc computational box, spanned by 1024^3 particles, starting at redshift $z = 100$. The cosmological parameters given by the *WMAP* 3-yr data have been adopted ($\Omega_{\rm M} = 0.24$, $\Omega_\Lambda = 0.76$, $h = 0.73$, $\Omega_{\rm b} = 0.0418$, $\sigma_8 = 0.75$, $n = 0.95$), giving a particle mass of $m_{\rm DM} = 1.63 \times 10^7\,h^{-1}\,\mathrm{M}_{\odot}$. (A more detailed description is provided in Zavala et al. 2009.)

In order to check the robustness of our results with respect to the particular realization of the constrained simulation, we also performed a second simulation with an independent underlying random realization. This second simulation implements the same constraints on the local structures at the present time. The simulation volume and number of particles are the same as above, while the background cosmology is now based on the *WMAP* 5-yr data, combined with the available constraints from the large-scale structure (baryonic accustic oscillations (BAO)) and supernovae ($\Omega_{\rm M} = 0.279$, $\Omega_\Lambda = 0.721$, $h = 0.73$, $\Omega_{\rm b} = 0.046$, $\sigma_8 = 0.817$, $n = 0.96$). In this case we include in the analysis not just the LG and Virgo, but also our other nearby galaxy cluster, Fornax. In Fig. 1 we show the local density distribution at redshift $z = 9$ within a slice of comoving $30\,h^{-1}$ Mpc $\times$ $30\,h^{-1}$ Mpc and $7\,h^{-1}$ Mpc depth which contains the progenitors of the objects of interest, Virgo, Fornax, M31 and Milky Way. The slice is situated in the supergalactic *YZ* plane. The main progenitors of these objects have at redshift $z = 9$ masses of 1.2×10^{11}, 6.6×10^{10}, 3.8×10^9 and $3.4 \times 10^9\,h^{-1}\,\mathrm{M}_{\odot}$, respectively. The marked Virgo (Fornax) regions are populated with about 2000 (700) cluster progenitors, each with a mass larger than $4 \times 10^8\,h^{-1}\,\mathrm{M}_{\odot}$. This leads to a total progenitor mass of $2.4 \times 10^{12}\,h^{-1}\,\mathrm{M}_{\odot}$ ($0.9 \times 10^{12}\,h^{-1}\,\mathrm{M}_{\odot}$). One can clearly see the low-density regions between the progenitors of the clusters and the progenitors of the LG. There are a few other objects next to the LG but with much smaller masses than that concentrated in the proto-cluster regions.

All our simulations were performed within the Constrained Local UniversE Simulations (CLUES) project.[1]

2.2 Radiative transfer simulations

The radiative transfer simulations were performed using a radiative transfer and non-equilibrium chemistry code called C^2-RAY

[1] http://clues-project.org

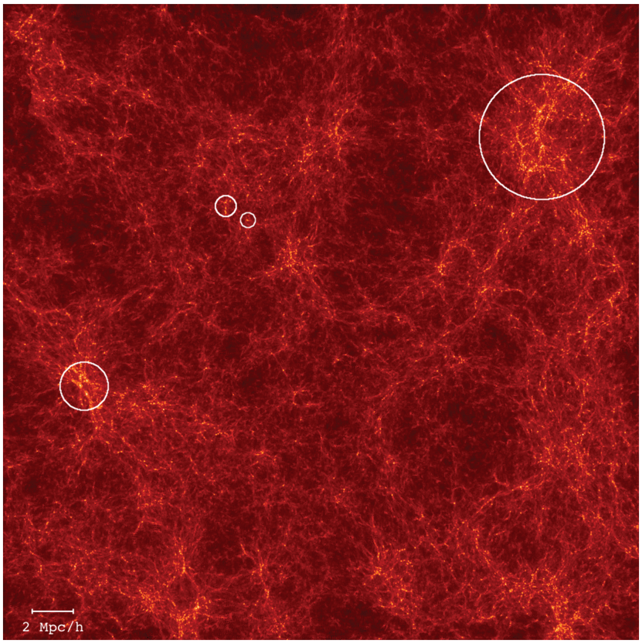

Figure 1. Matter distribution in a volume of $30\,h^{-1}$ Mpc × $30\,h^{-1}$ Mpc × $7\,h^{-1}$ Mpc depth in comoving Mpc at redshift $z = 9$. The circles with decreasing radius according to the decreasing mass of the objects denote the regions where the progenitors of Virgo, Fornax, M31 and Milky Way are situated. The slice is situated in the supergalactic *YZ* plane.

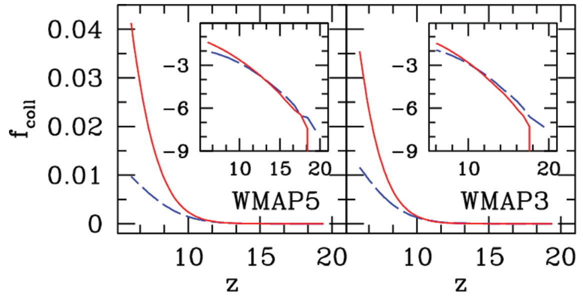

Figure 2. Collapsed fraction in high-mass ($M > 10^9\,\mathrm{M}_\odot$; red, solid) and low-mass sources ($M < 10^9\,\mathrm{M}_\odot$; blue, dashed) (insets show the same in log scale) versus cosmic redshift for *WMAP*5 (left) and *WMAP*3 (right) cases.

(Mellema et al. 2006a), tested in detail as discussed in Mellema et al. (2006a), Iliev et al. (2006b) and Iliev et al. (2009). Our simulation methodology was presented in Iliev et al. (2006a), Mellema et al. (2006b) and Iliev et al. (2007). The underlying *N*-body structure formation simulations discussed in the previous section provide a time sequence of density distributions and catalogues of identified haloes. Gas is assumed to follow the dark matter distribution, which at these scales (0.25–64 h^{-1} Mpc) is a very good approximation. We have produced 53 density slices and halo catalogues roughly equally spaced in time between the redshifts 20 and 6, every ∼14.5 Myr. All haloes are assumed to host galaxies and thus to be potential sources of ionizing radiation. Each is assigned an ionizing luminosity proportional to its mass. Low-mass sources, with total mass below $10^9\,\mathrm{M}_\odot$, are assumed to be active in the neutral regions, but to be suppressed in the ionized regions. Therefore, once their cell is ionized their emissivity is set to zero. These assumptions are based on the fact that the Jeans mass rises significantly when a region is ionized and heated, which thereby limits the fresh gas infall on to haloes and suppresses the future formation of low-mass galaxies; see Iliev et al. (2007) for a more detailed discussion.

Both the density and haloes are binned on a 256^3 grid for the radiative transfer processing. Haloes in the same radiative transfer (RT) cell are combined and a luminosity is assigned following a simple, physically motivated prescription. The emissivity of the ionizing sources – how many ionizing photons produced in galaxies over some time period reach the intergalactic medium – depends on what fraction of the galactic gas is converted into stars, how effective are the stars at producing ionizing photons and, finally, what fraction of the photons manage to escape the galaxy. We parametrize it with a single parameter f_γ, which is equal to the number of ionizing photons per atom in galaxies which reach the intergalactic medium in the time between two consecutive time slices.[2] The main difference between our two adopted background cosmologies is in the density fluctuation normalization (σ_8). A higher σ_8 yields higher halo collapsed fractions at any given epoch and a correspondingly larger number of collapsed haloes, as illustrated in Fig. 2. In terms of reionization this means that for a fixed ionizing emissivity proportional to the collapsed fraction the evolution is shifted to somewhat earlier times, resulting in an earlier overlap epoch (Alvarez et al. 2006). This effect was much larger for *WMAP* 1-yr ($\sigma_8 = 0.9$) versus *WMAP* 3-yr data ($\sigma_8 = 0.74$) than it is for *WMAP* 5-yr data ($\sigma_8 = 0.8$) versus the *WMAP* 3-yr data.

Much larger uncertainty concerns the properties of high-redshift sources. Because of the still scarce observational data those are not at well constrained at present and hence f_γ is largely a free parameter within certain, fairly wide, bounds. Furthermore, the radiative transfer simulations are quite computationally expensive, and therefore it is not practical to investigate the full available parameter space. We address this problem by considering two representative cases which are roughly bracketing the range of expected behaviour, while at the same time satisfying the available global observational constraints, as follows. For our Model 1 simulation we use the first *N*-body realization, with *WMAP*3 cosmology and we adopt $f_\gamma = 100$ for the massive sources ($M > 10^9\,\mathrm{M}_\odot$) and $f_\gamma = 250$ for the low-mass, suppressible ones ($M < 10^9\,\mathrm{M}_\odot$). These relatively high efficiencies yield a fairly fast, photon-rich reionization process with an early overlap. For our second simulation, on the other hand, we use the second constrained realization, with *WMAP*5 cosmology, and we adopt lower source efficiencies of $f_\gamma = 10$ for the massive sources and $f_\gamma = 150$ for the low-mass ones. This yields a more extended, photon-poor reionization history. For conciseness of notation, we will refer to the two combinations of *N*-body realizations and corresponding radiative transfer simulation simply as the Model 1 and Model 2 cases, with the implicit understanding that this implies a different constrained realization and assumed photon emissivities of the sources, as well as different background cosmology.

3 RESULTS

3.1 Global reionization history

The global mass-weighted reionization histories produced by our two simulations are shown in Fig. 3. In either case reionization

[2] One can also introduce a slightly different efficiency parameter, g_γ, given by $g_\gamma = f_\gamma \left(\frac{10\,\mathrm{Myr}}{\Delta t}\right)$ where Δt is the time between two snapshots from the *N*-body simulation. This has the advantage that it is a rate per unit time and as such it is independent of Δt, which makes easier comparisons between simulations with different Δt.

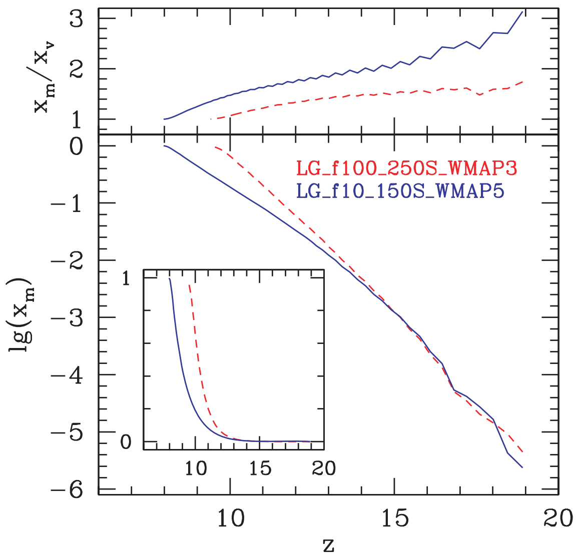

Figure 3. Bottom: evolution of the mass-weighted ionized fractions, x_m for Model 1 (red, dashed) and Model 2 (blue, solid) cases, inset shows the same in linear scale. Top: the corresponding ratios of mass-weighted to volume-weighted ionized fractions, which corresponds to the average density of the ionized regions in units of the mean, versus redshift z.

starts when the first resolved haloes (which correspond to the first ionizing sources) form, around $z \sim 20$.

Our adopted f_γ values yield final overlap of ionized regions at $z_{\rm ov} \sim 9$ (8) for the Model 1 (Model 2) case, in rough agreement with the current observational constraints. The corresponding integrated Thomson scattering optical depth seen by the cosmic microwave background photons, $\tau_{\rm es} = 0.094(0.069)$, is also in agreement with the latest constraints from *WMAP* satellite combined with the other available data sets, $\tau_{\rm es} = 0.084 \pm 0.016$ (Komatsu et al. 2009).

Additional constraints on reionization and its sources come from recent measurements of the mean optical depth of the Lyα forest around and after overlap (e.g. Bolton & Haehnelt 2007; Becker et al. 2011). A combination of proximity effect measurements for high-redshift QSOs and detailed numerical simulations implies that reionization, at least during its late stages, was likely photon-starved, with a mean derived IGM photoionization rate (which could be related to the measured mean IGM optical depth) of $\Gamma_{-12} \lesssim 1$ at $z \sim 6$. Both of our models yield mean IGM photoionization rates at overlap similar to the measured value, but rise quickly post-overlap, possibly violating this observational constraint, particularly for the photon-rich Model 1. However, imposing the Lyα forest constraints properly would require higher resolution, gasdynamics, and, most importantly, a correct treatment of the Lyman-limit systems (LLS). The latter are optically thick systems which regulate the mean free path of the ionizing photons after overlap. The abundances and even nature of these systems at high redshift is still highly uncertain, making them difficult to model numerically. Furthermore, the high-redshift photoionization rate measurements are extremely difficult and the values obtained contain significant uncertainties. Given these uncertainties, we consider both of our models to be viable, keeping in mind that the Lyα forest constraints likely give preference to the photon-poor models of reionization. We also note that before overlap the mean free path of the ionizing photons is dominated by the remaining neutral patches and therefore lack of LLS modelling in our simulations does not affect our results below.

The early reionization ($z > 14$) is driven primarily by the low-mass sources, which have similar efficiencies in the two cases (the slightly lower source efficiency in the Model 2 case is compensated for by its higher collapsed fraction at the same redshift) and as a consequence the two reionization histories are initially very similar. Later on the larger sources take over, both because of their rapidly rising collapsed fraction (cf. Fig. 2) and the strong Jeans suppression of the low-mass sources, and thus reionization proceeds more slowly in the Model 2 case due to the lower efficiency adopted for its high-mass sources. The fact that the mean mass-weighted ionized fraction, x_m, is always larger than the corresponding volume-weighted one, x_v (Fig. 3, upper panel), indicates that reionization proceeds in an inside-out fashion (i.e. high-density regions are preferentially ionized first) in both cases, in agreement with previous simulation results based on non-constrained realizations (Iliev et al. 2006a). For the Model 2 realization this ratio is noticeably higher, up to $\sim$3 at $z = 20$, due to its more advanced structure formation at any given redshift. This also boosts the clumpiness of the gas, and therefore the recombinations, which in turn extends reionization even further.

3.2 Local reionization histories

The mean reionization history presented above ensures that the currently available global observational constraints – the electron-scattering optical depth and overlap epoch are satisfied. However, to achieve our present goals we need to track separately the reionization history of the progenitors of each object of interest, namely the LG, as well as the nearby clusters of galaxies. To this purpose, we extracted the Lagrangian mass distribution for each object (i.e. the mass which eventually will end up in that object by the present day) and followed the reionization history of all radiative transfer cells containing at least one particle which ends up in that object by $z = 0$. The resulting local reionization histories are shown in Fig. 4, along with the global one for direct comparison.

The Lagrangian regions of both the LG and the nearby clusters are significantly overdense in either constrained realization and at all times, reflecting the fact that all of these objects correspond to high peaks of the density field. The proto-LG region starts only moderately overdense, by $\sim$7 per cent ($\sim$9 per cent) in the Model 1 (Model 2) case, which rises over time as the corresponding object collapses gravitationally, to reach $\sim$16 per cent ($\sim$25 per cent) by the global overlap epoch at $z \sim 9$ (8). The proto-clusters correspond to still higher peaks of the density field. Initially the proto-Virgo region is overdense by 12 per cent for both simulations, rising over time to 24 per cent (30 per cent) for Model 1 (Model 2). The proto-Fornax region (Model 2) starts 10 per cent overdense, rising to 26 per cent by the global overlap. The higher local density yields an (exponentially) larger halo collapsed fraction and thus ionizing photon production. Therefore, for both LG and clusters we can expect local reionization to occur earlier than average, which is confirmed by our simulation results (Fig. 4).

In both simulations the LG reionization starts at about $z \sim 12.5$, at which time its oldest progenitor haloes form. Before $z \sim 12.5$ the LG ionized fraction is tiny, below 3×10^{-9} (2×10^{-5}) for Model 1 (Model 2). Thereafter the (proto-)LG reionization accelerates, albeit only gradually. For Model 1 (Fig. 4, left) the LG ionized fraction reaches 17 per cent by $z \sim 12$ and 39 per cent by $z \sim 10.5$. After that point the evolution becomes very fast and full ionization ($x_m >$ 99 per cent) is achieved by $z \sim 10$. In contrast, the reionization history of the (proto-)Virgo cluster in the same Model 1 simulation is quite different. Proto-Virgo is a higher density peak and the

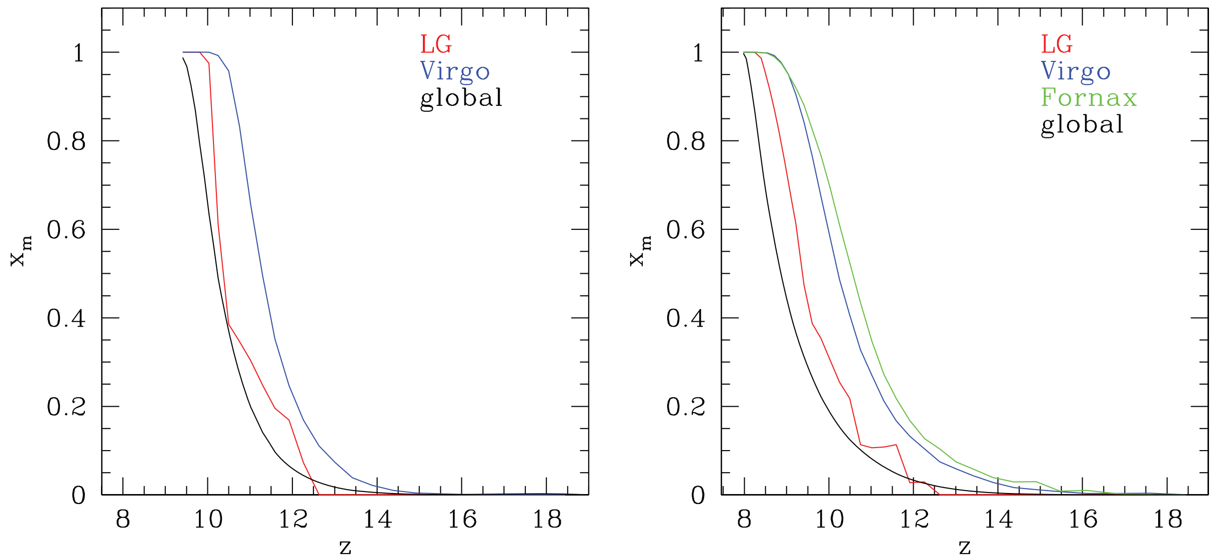

Figure 4. Mass-weighted mean ionized fractions, x_m, for the Local Group, nearby clusters and global mean (as indicated by colour) versus redshift for Model 1 (left; left to right: global, LG, Virgo) and Model 2 (right; left to right: global, LG, Virgo, Fornax).

formation of the local non-linear structures is therefore accelerated. Hence the local reionization proceeds faster, as well. The evolution remains smooth throughout, with no sudden changes of slope, unlike in the LG case. The mass-weighted ionized fraction reaches 11 per cent by $z = 12.6$, 50 per cent by $z = 11.3$ and 96 per cent by $z = 10.5$.

The reionization histories are similar in the Model 2 case (Fig. 4, right). Once again, the proto-cluster regions, both Virgo and Fornax, reionize earlier than LG and much earlier than an average region – $x_m = 0.1$ is reached by $z = 12.3$ (12.6), $x_m = 0.5$ by $z = 10.25$ (10.5) and $x_m = 0.9$ by $z = 9.2$ (9.3) for Virgo (Fornax). For both proto-clusters overlap ($x_m = 0.99$) is reached at $z = 8.7$ and the evolution remains smooth throughout. Interestingly, most reionization stages (but not the local overlap, which is roughly simultaneous) of the Fornax reionization occur earlier than the corresponding ones for Virgo, even though Fornax has lower mass at the present epoch. In comparison, the reionization of the LG occurs later, reaching $x_m = 0.1$ by $z = 11.6$, $x_m = 0.5$ by $z = 9.4$, $x_m = 0.9$ by $z = 8.6$ and local overlap is achieved by $z = 8.4$. It lags the global mean in its earliest stages ($z > 12.5$), but as more progenitor haloes form it catches up and then speeds ahead after $z = 12$. The LG reionization history is again much less smooth than the proto-cluster ones, with significant changes of slope at $z \sim 12$, 11 and 9.6. Evolution becomes extremely fast after $z \sim 9.6$, whereby the ionized mass fraction jumps from 0.4 to 1 over a redshift interval of just $\Delta z \sim 1$. Compared to the Model 1 case the reionization histories for Model 2, both mean and local ones, are much more extended in time due to the lower source emissivities assumed .

Moving on to a more visual representation of the local reionization history, in Fig. 5 we show a 3D volume rendering of the distribution of mass which is destined by the present time ($z = 0$) to become part of the LG and nearby clusters for Model 1 at $z = 10$ (left) and for Model 2 at $z = 9$ (right). In the realization corresponding to Model 1 the proto-Virgo is a quite large, elongated object, extending for about 10 × 20 comoving Mpc, which corresponds to about 1 proper Mpc at this early time, while the proto-LG is a much smaller object a few Mpc in size, about 7 comoving Mpc (less than 1 physical Mpc) away from proto-Virgo. In the alternative Model 2 realization the size of the proto-LG and its distance from Virgo are similar to those for the Model 1 realization. However, the

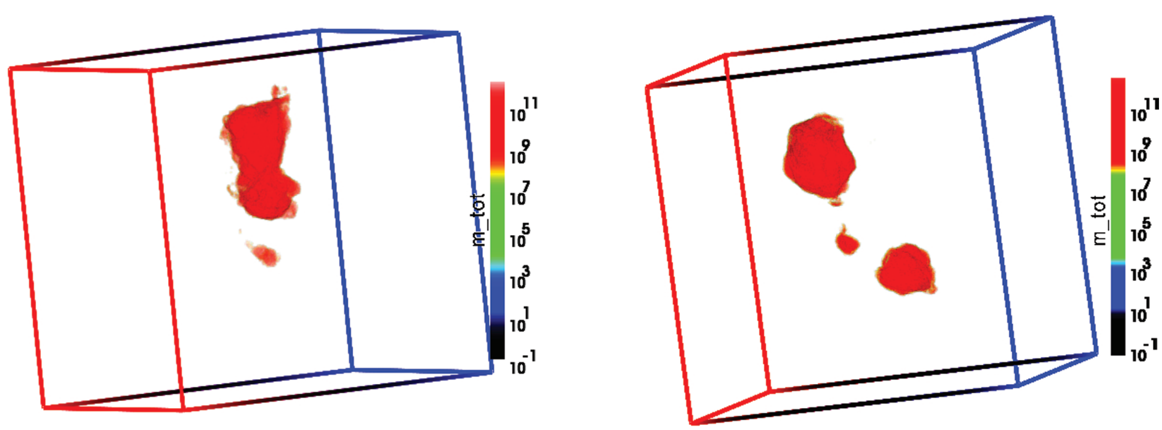

Figure 5. Volume rendering of the total mass, which by the present time ($z = 0$) will end up as part of the objects of interest here: (left) Virgo cluster (top object) and the Local Group (bottom object) at redshift $z = 10$; (right) Virgo cluster (top object), the Local Group (middle, smaller object) and Fornax (bottom object) at redshift $z = 9$. The colour scale units are solar masses per radiative transfer cell.

proto-Virgo is a more compact, less extended object and a proto-Fornax is identified, as well, at a similar distance from the LG, positioned in almost diametrically opposite direction. Proto-Fornax is a somewhat less extended object than proto-Virgo.

In Figs 6 and 7 we show the evolution of the neutral mass remaining in the objects of interest in a time sequence for simulations for Model 1 and Model 2, respectively. In each case the sequence covers the key time interval during which most of the LG material is ionized. In Model 1 at $z = 10.75$ the reionization of Virgo is already well advanced, with a local ionized fraction above 83 per cent, while LG remains largely neutral, at less than 35 per cent. Shortly thereafter, an ionization front arrives at the proto-LG position from the direction of Virgo and quickly sweeps through it as illustrated by the next three images. This corresponds to the dramatic jump of the LG local ionized fraction seen in Fig. 4 at $z =$ 10.5–10.25. By $z = 10$ the LG material is almost fully ionized, reaching 97.5 per cent ionized fraction by mass. In this case, therefore the LG is largely ionized from the outside, primarily by the Virgo progenitors.

The evolution proceeds quite differently in the photon-poor, Model 2, case, as illustrated in Fig. 7. While the nearby clusters, in this case both Virgo and Fornax, once again reionize themselves from the inside and relatively earlier than the LG, there are no clear ionization fronts to arrive from them and sweep over the LG material. The LG internal sources carve ionized bubbles from the inside and eventually manage to reionize all the LG materials mostly by themselves. While we cannot exclude modest contributions from Virgo and Fornax, the local LG sources appear to dominate the evolution in this case.

In order to evaluate the local reionization process for each structure in a more quantitative way, we counted and added up all ionizing photons emitted by sources within the same Lagrangian volume, normalized by the total number of atoms belonging to that object. We also counted and added together the cumulative number of ionizing photons used up to ionize each object of interest and also to keep it ionized (i.e. recombinations, since after each recombination back to neutral state that atom would need to be ionized again), again normalized per atom in that object . Comparing the values of these two numbers over time shows if that particular object by itself produced enough photons up to that point in time to fully account for its current ionization state. Results for both models are shown in Fig. 8.

The results confirm our conclusions based on the visual examination of the reionization process we discussed above. The galaxy clusters initially produce most of the photons needed for their own reionization. Until $z \sim 10.5$ ($z \sim 9$–9.5) for Model 1 (Model 2) there is some deficit of photons, i.e. a little more are used up than produced by the progenitors of that cluster. The reason for this is that clusters are located at high peaks of the density field, and it is well established that CDM haloes, and thus our ionizing sources, strongly cluster around such high peaks. As a consequence of that there are many nearby sources which surround the proto-cluster region and contribute to its reionization. However, we note that the final overlap in each case is only reached after the cluster itself has produced sufficient number of photons. We also note that recombinations have a very significant effect for proto-clusters, yielding usage of 1–1.5 additional ionizing photons per atom in addition to the one photon needed to achieve the initial ionization of that atom.

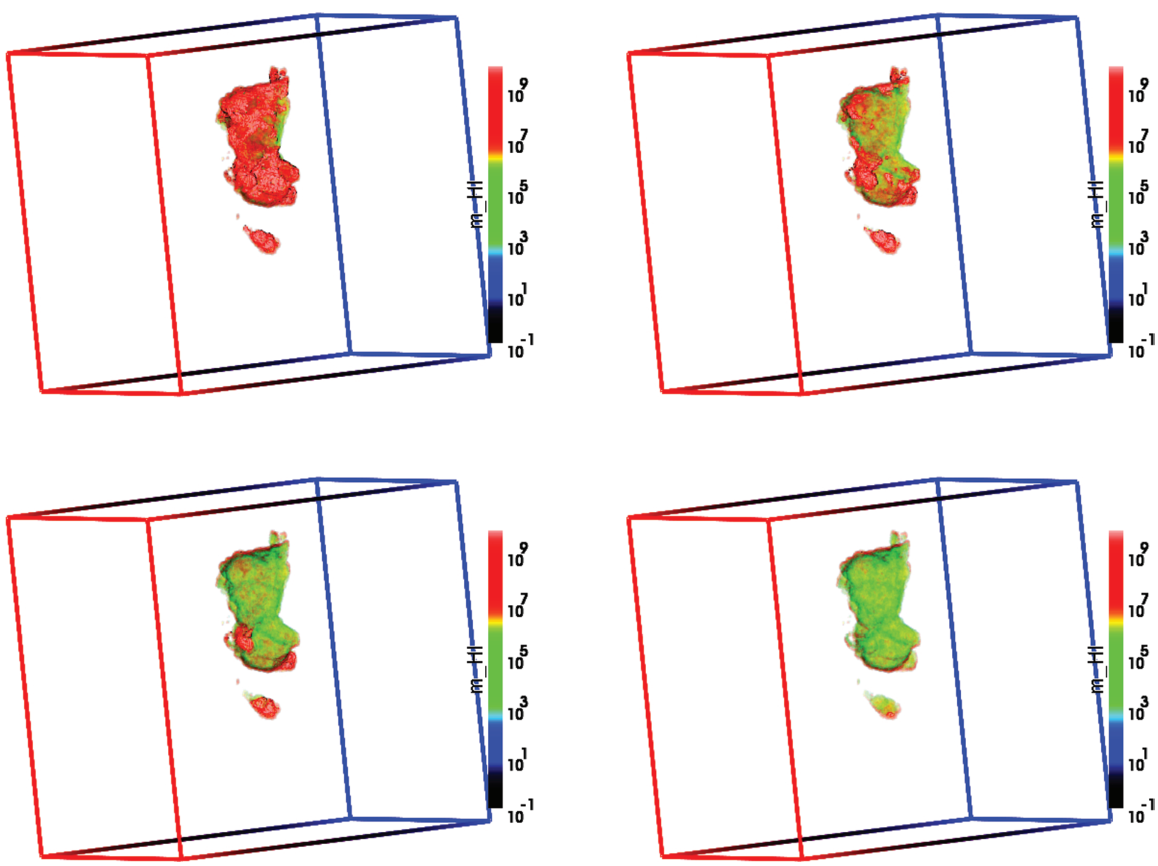

Figure 6. Evolution of the neutral mass at (top to bottom and left to right) redshifts $z = 10.75$, 10.5, 10.25 and 10 for Model 1. Red is neutral, green is ionized.

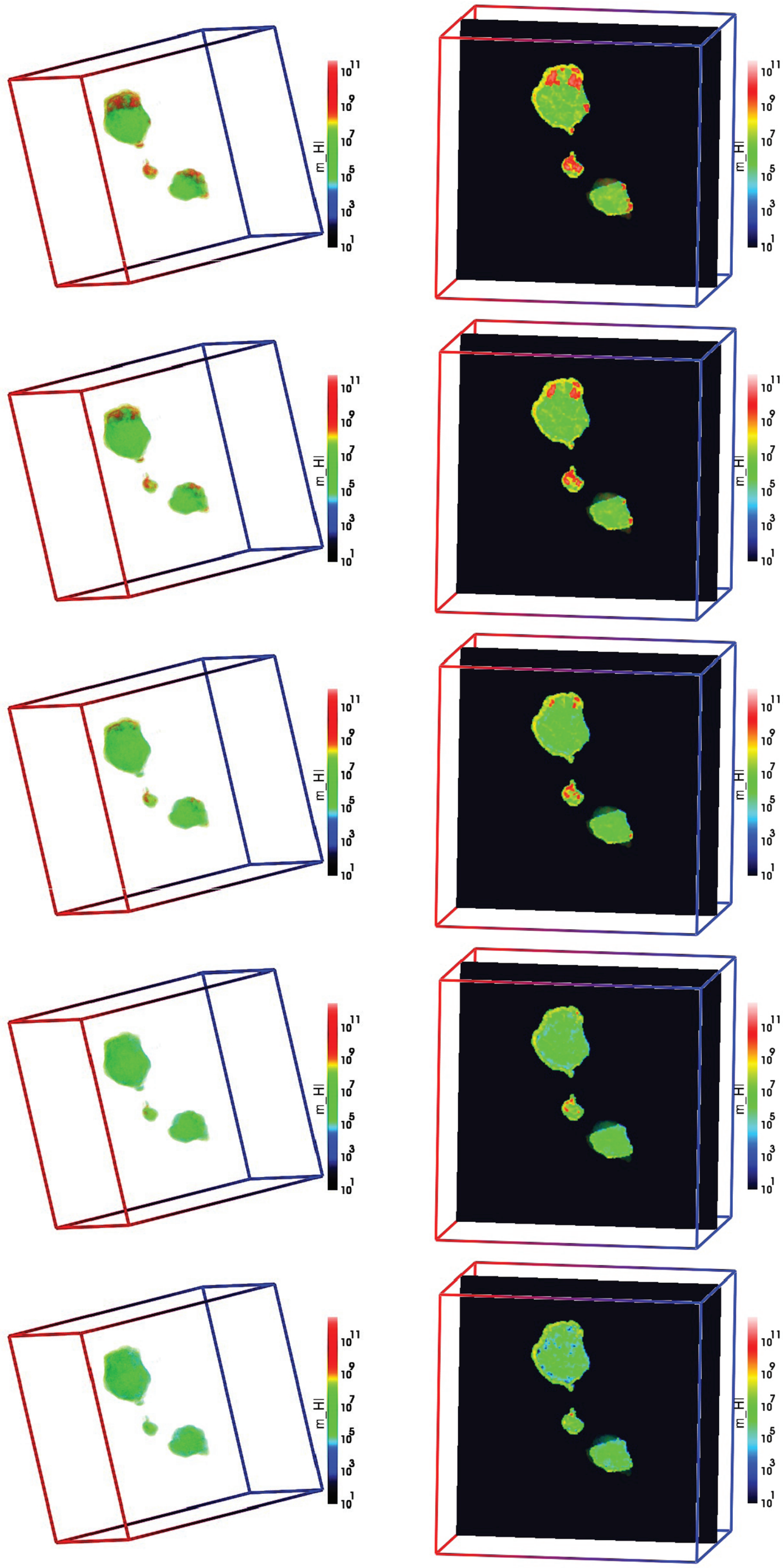

Figure 7. Evolution of the neutral mass at (top to bottom) redshifts $z = 9, 8.9, 8.7, 8.55$ and 8.4 in 3D volume rendering (left) and cross-section (right) for Model 2. Red is neutral, green/blue is ionized.

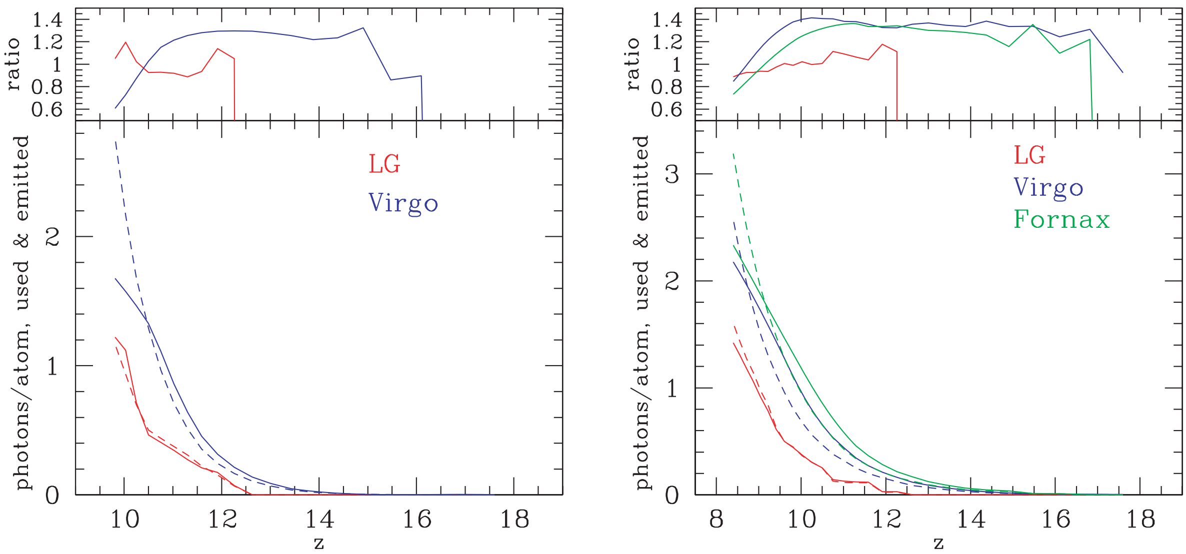

Figure 8. Cumulative number of ionizing photons for ionizations and recombinations (solid) and photons emitted (dashed), both per atom, for the Local Group and nearby clusters (as indicated by colour) versus redshift for Model 1 (left-hand panel) and Model 2 (right-hand panel).

On the other hand, the proto-LG results are different from the cluster results in both cases. In the photon-rich Model 1 up to $z \sim 10.5$ there are exactly as many photons produced by the LG progenitors as are used up for its own reionization. After that point however there is a significant change of slope for both curves. Suddenly there are clearly more photons arriving than are produced locally. This change of slope occurs exactly when the ionization front from Virgo was seen above to sweep through the LG material. The number of photons used for ionizations and recombinations is above the number of locally emitted photons and it remains so up to the redshift of full reionization (i.e. local overlap) of the LG, $z \sim 10$. This behaviour is more clearly seen in the top panel of Fig. 8 (left), where we show the ratio of photons used over photons emitted locally for the LG and Virgo. This ratio starts above one at $z \sim 12.3$–11.7, indicating that the early LG reionization is partially helped along by nearby sources that do not belong to it. However, this photon ratio then falls slightly below 1 and remains so until $z = 10.5$. At this point the external ionization front arrives and the ratio jumps to well above 1, peaking at 1.2 and remaining above 1 until the local overlap. We therefore conclude that in this case most of the LG gas (up to 70 per cent, see Fig. 4) was indeed reionized externally, predominantly by the nearby Virgo cluster.

In our Model 2 (photon-poor) case the photon budgets of the proto-clusters Virgo and Fornax are very similar to each other as well as to that of proto-Virgo in our Model 1. There is a noticeable contribution of photons from nearby clustered sources, which supply at least 40 per cent more photons than the respective internal sources. However, after $z \sim 10$ (when Virgo is 60 per cent ionized and Fornax is 70 per cent ionized) the ratio of consumed over produced photons drops quickly and by their full ionization ($z = 8.7$) both clusters have internally produced more photons than are needed for their own ionization. The local recombinations have a significant effect, resulting in about one additional photon per atom needed to keep them ionized.

In contrast, the ionizing photons which are produced locally by the LG progenitors roughly balance the ones consumed for its own reionization all the way up to its neighbourhood overlap at $z \sim 8.4$. Once again initially (at $z > 11$) there is some external contribution of ionizing photons from nearby sources, but in this case throughout most of the evolution ($8.4 < z < 11.5$) the emitted and consumed photons balance within less than 10 per cent. In fact, at the later stages of the evolution the LG progenitor haloes produce a bit more photons than are actually used to ionize it and keep it ionized. Hence, the LG evolves largely isolated in this case. After the local overlap the LG produces even more photons than are actually needed to keep it ionized. The effect of recombinations on the LG reionization history is more modest than in the case of the proto-clusters, resulting in only about 0.5–0.8 additional photons being consumed in either simulation, in agreement with the lower overdensity of the LG region. Based on these results we therefore can conclude that in the photon-poor Model 2 the reionization of both the LG and the nearby clusters is mostly a local process, with no significant external contributions from other structures.

4 SUMMARY AND CONCLUSIONS

We have performed the first simulations of the reionization history of our local neighbourhood of the universe based on constrained N-body simulations of the formation of local structures – our LG of galaxies and the nearby galaxy clusters. The reionization history of the LG cannot yet be predicted uniquely, primarily due to the still poor observational constraints on the properties of the reionization sources. Therefore, we studied two models constructed so as to roughly bracket the range of expected outcomes. While both models roughly satisfy the available global observational constraints on the integrated electron scattering optical depth and overlap epoch, they differ significantly in their underlying assumptions. Our first model assumes relatively high ionizing photon production efficiencies (‘photon-rich reionization’), while our second model studies the other extreme, where the sources produce barely enough photons to complete the reionization process in time (‘photon-poor reionization’). The second model therefore results in more extended reionization history and delayed final overlap. As noted in Section 3.1, other observational constraints on reionization based on the Lyα forest likely give preference to the more extended, photon-poor end of the spectrum of reionization efficiencies. Our two bracketing case models have the same observational constraints imposed on their initial matter distribution, which guarantees that the large-scale structures closely resemble our local neighbourhood, but they differ in their random component, yielding different constrained realizations. This allows us to check the robustness of our results with respect to the specific realization. Finally, the two models also have different underlying cosmological models (*WMAP* 3-yr versus *WMAP* 5-yr best fit). However, the effect of the background cosmology is well understood and results in an overall shift of the reionization earlier or later, with no significant effects on our results, for which only the relative timing of structure formation versus reionization history is of importance.

Our results show that the assumed efficiency of the ionizing sources has the most important influence on the nature of the reionization history of our LG of galaxies. Efficient photon production ensures that the nearby clusters emit more than sufficient number to ionize both themselves and their surroundings, including the LG. The fact that those galaxy clusters (Virgo and Fornax) coincide with high, rare peaks of the density field means that they form their progenitor haloes earlier than the LG, which is in a more average region of the universe. As a result, the large-scale ionization fronts which propagated outward from the proto-clusters overrun the LG before it managed to form enough sources to ionize itself, resulting in its reionization being mostly externally driven.

Several points are worth noting here. Although generally the radiative transfer is a highly non-local phenomenon (a feature which complicates its numerical treatment and the code parallelization) during most of the epoch of reionization (EoR) the situation is somewhat more complicated. The neutral patches have enormous optical depth to soft ionizing radiation (the only type of radiation we consider here). Even the already-ionized patches still have considerable continuum optical depth over cosmological (multiple Mpc) distances due to the small residual neutral fraction still remaining in such regions.[3] This residual neutral fraction diminishes over time, but does so only gradually, as more and more sources appear and the mean flux thereby increases. As a consequence of all this, reionization starts out as a fairly local process where only the relatively nearby, directly visible ionizing sources within the same ionized bubble contribute to the flux at a given point. This property allows us to focus our analysis on the important local sources and ignore the far-away ones for our current purposes (they are of course all included in the radiative transfer simulation). In our $\sim$100 Mpc box there are multiple proto-clusters which collapse non-linearly by the present, but of those only Virgo and Fornax are sufficiently close to potentially contribute to the reionization of our LG.

Furthermore, the ionization fronts propagate through underdense regions (voids) much faster than through overdense ones (filaments, knots). Therefore, the relative positioning of the structures of interest and the density fluctuations in their immediate neighbourhood are important. Once the available observational constraints are imposed in order to reproduce the local structures, we find that the LG is separated from Virgo and Fornax by voids in either realization (see Fig. 1). In contrast, the previous studies of this problem which did not use constrained realizations (Weinmann et al. 2007; Alvarez et al. 2009) sampled a wide range of environments and relative positions of nearby clusters. Such a purely statistical approach yields valuable insights on the range of reionization histories that could be expected for a certain type of object (e.g. LG-like objects). However, by its nature such an approach necessarily includes many objects which, although they share certain basic features, locally do not reproduce the specific large-scale structures around us. Therefore, the constrained realizations are indispensable if we want to make reliable predictions for the effects of reionization on our neighbourhood.

Why is the mode of reionization, external versus internal, of our LG an important issue? This has a number of implications for the formation of structures. Reionization dramatically rises the Jeans mass, thus impeding the formation and growth of small galaxies. In terms of this effect, the galactic haloes fall into three categories. The smallest haloes (minihaloes) have virial temperatures below the limit ($\sim 10^4$ K) for efficient radiative cooling through atomic line radiation. The ionization of the gas brings its temperature to $\sim 10^4$ K and it boils out, resulting in their complete evaporation (Shapiro, Iliev & Raga 2004; Iliev, Shapiro & Raga 2005), which leaves behind dark haloes. In the other limit, the galaxies above certain mass ($M \gtrsim 10^{10}\,\mathrm{M}_\odot$) have sufficiently deep gravitational potential wells to successfully withstand the effects of ionizing radiation and are thus not significantly affected by the reionization process. The effects of radiative feedback on dwarf galaxies of intermediate mass, roughly between 10^8 and $10^{10}\,\mathrm{M}_\odot$, is more complex. The gas in such already-formed systems cannot be photoevaporated, as it can cool back down to $\sim 10^4$ K very efficiently. However, photoionization heating rises the intergalactic gas temperature and pressure, which rises the Jeans mass and thereby suppresses the future formation of very low mass galaxies, as well as curtails the fresh gas infall on to such haloes. Larger galaxies are less affected directly, but could do so indirectly, through their smaller progenitors, which could be expected e.g. to result in smoother gas substructure and modified stellar populations. Where the boundary between efficient and inefficient feedback from reionization lies is still unclear and very much subject of active research. Full investigation of the effects of reionization on galaxy formation and satellite galaxy populations goes well beyond the scope of this paper. However, our present results indicate that the photon production efficiencies of the first galaxies are the main factor determining the type of reionization history which our LG underwent. In our Model 1 at the time of its reionization the LG galaxies (the Milky Way, M31 and M33) have 39 progenitors large enough to survive reionization (half of them are part of the proto-Milky Way), and a similar number (30 +) of progenitors survive in Model 2. Some of these progenitors later merge to form the present-day objects, while others would remain as satellite galaxies. Our current simulations do not have sufficient resolution to follow this evolution in detail and determine how many of these surviving dwarf galaxies remain as satellites and how many merge into the present-day objects. Furthermore, the smallest haloes resolved in our simulations have mass of $5 \times 10^8\,\mathrm{M}_\odot$, while, as discussed above, some smaller objects, possibly as small as $10^8\,\mathrm{M}_\odot$, could survive reionization, as well. Further, much higher resolution simulations are required to settle these questions and provide a complete statistics of the primordial satellite galaxies. This could also provide direct observational evidence for the radiative feedback and suppression of low-mass galaxies by other low-mass galaxies during reionization. These processes should therefore have left useful fossil records in the properties of our neighbourhood which will help us use local observations to answer some of the key questions about the young universe.

ACKNOWLEDGMENTS

This study was supported in part by Swiss National Science Foundation grant 200021-116696/1 and Swedish Research Council

[3] For example, at redshift $z = 8$, for mean density and residual neutral fraction of 10^{-3}, the mean free path is $\sim$3 Mpc. Density fluctuations further diminish this value.

grant 60336701. GY acknowledges support of MICINN (Spain) through research grants FPA2009-08958, AYA2009-13875-C03-02 and CONSOLIDER-INGENIO SyEC (CSD2007.0050). YH has been partially supported by the ISF (13/08). The CLUES simulations have been performed in the MareNostrum supercomputer at BSC (Spain) and the HLRBII Altix computer at LRZ (Germany). We also thank DEISA for granting us CPU time in these computers through two DECI projects SIMU-LU and SIMUGAL-LU. We thank Nick Gnedin for making publicly available his visualization code IFRIT, which was used to produce the images in Figs 4–6. Some of the radiative transfer simulations were run on SNIC computing time at HPC2N (Umeå, Sweden). We thank Kristin Riebe for providing Fig. 1 made with PMVIEWER[4] of Arman Khalatyan.

REFERENCES

Alvarez M. A., Shapiro P. R., Ahn K., Iliev I. T., 2006, ApJ, 644, L101
Alvarez M. A., Busha M., Abel T., Wechsler R. H., 2009, ApJ, 703, L167
Becker G. D., Bolton J. S., Haehnelt M. G., Sargent W. L. W., 2011, MNRAS, 410, 1096
Bolton J. S., Haehnelt M. G., 2007, MNRAS, 382, 325
Bullock J. S., Kravtsov A. V., Weinberg D. H., 2000, ApJ, 539, 517
Busha M. T., Alvarez M. A., Wechsler R. H., Abel T., Strigari L. E., 2010, ApJ, 710, 408
Gottlöber S., Hoffman Y., Yepes G., 2010, in Wagner S., Steinmetz M., Bode A., Müller M., eds, Proc. High Performance Computing in Science and Engineering, Constrained Local UniversE Simulations (CLUES). Springer, Berlin, p. 309
Hoffman Y., Ribak E., 1991, ApJ, 380, L5
Iliev I. T., Shapiro P. R., Raga A. C., 2005, MNRAS, 361, 405
Iliev I. T., Mellema G., Pen U.-L., Merz H., Shapiro P. R., Alvarez M. A., 2006a, MNRAS, 369, 1625
Iliev I. T. et al., 2006b, MNRAS, 371, 1057
Iliev I. T., Mellema G., Shapiro P. R., Pen U.-L., 2007, MNRAS, 376, 534
Iliev I. T. et al., 2009, MNRAS, 400, 1283
Karachentsev I. D., Karachentseva V. E., Huchtmeier W. K., Makarov D. I., 2004, AJ, 127, 2031
Klypin A., Hoffman Y., Kravtsov A. V., Gottlöber S., 2003, ApJ, 596, 19
Komatsu E. et al., 2009, ApJS, 180, 330
Macciò A. V., Kang X., Fontanot F., Somerville R. S., Koposov S., Monaco P., 2010, MNRAS, 402, 1995
Mackey J., Bromm V., Hernquist L., 2003, ApJ, 586, 1
Mellema G., Iliev I. T., Alvarez M. A., Shapiro P. R., 2006a, New Astron., 11, 374
Mellema G., Iliev I. T., Pen U.-L., Shapiro P. R., 2006b, MNRAS, 372, 679
Muñoz J. A., Madau P., Loeb A., Diemand J., 2009, MNRAS, 400, 1593
Reiprich T. H., Böhringer H., 2002, ApJ, 567, 716
Shapiro P. R., Iliev I. T., Raga A. C., 2004, MNRAS, 348, 753
Springel V., 2005, MNRAS, 364, 1105
Tonry J. L., Dressler A., Blakeslee J. P., Ajhar E. A., Fletcher A. B., Luppino G. A., Metzger M. R., Moore C. B., 2001, ApJ, 546, 681
Weinmann S. M., Macciò A. V., Iliev I. T., Mellema G., Moore B., 2007, MNRAS, 381, 367
Willick J. A., Courteau S., Faber S. M., Burstein D., Dekel A., Strauss M. A., 1997, ApJS, 109, 333
Zahn O., Lidz A., McQuinn M., Dutta S., Hernquist L., Zaldarriaga M., Furlanetto S. R., 2007, ApJ, 654, 12
Zavala J., Jing Y. P., Faltenbacher A., Yepes G., Hoffman Y., Gottlober S., Catinella B., 2009, ApJ, 700, 1779

[4] http://pmviewer.sourceforge.net/

This paper has been typeset from a TEX/LATEX file prepared by the author.